Density-Gradient Analysis for Density Functional Theory: Application to Atoms*

ALEŠ ZUPAN

Department of Environmental Chemistry, ''Jožef Stefan'' Institute, Jamova 39, 61111 Ljubljana, Slovenia

JOHN P. PERDEW AND KIERON BURKE

Department of Physics and Quantum Theory Group, Tulane University, New Orleans, Louisiana 70118

MAURO CAUSÀ

Department of Inorganic Chemistry, University of Torino, Via Pietro Giuria 5, I-10125, Torino, Italy

Received September 15, 1995; revised manuscript received March 13, 1996; accepted March 19, 1996

ABSTRACT

We present an analysis of local or semilocal density functionals for the exchange–correlation energy by decomposing them into their gradients r_s (local Seitz radius), ζ (relative spin polarization), and s (reduced density gradient). We explain the numerical method pertaining to this kind of analysis and present results for a few atoms and ions. The atomic shell structure is prominent, and only the ranges $0 < r_s < 10$ and $0 < s < 3$ are important. The low-density and large-gradient domains, where the approximations for the exchange–correlation energy are least trustworthy, have very little weight.

*Presented at the Paris DFT 95 Conference.

International Journal of Quantum Chemistry, Vol. 61, 835–845 (1997)

CCC 0020-7608 / 97 / 050835-11

Introduction

Use of density functional theory to predict the ground state of an electronic system depends on the level of approximation for the exchange–correlation energy, which includes all the many-body effects and so cannot be calculated exactly. The simplest approximation for the exchange–correlation energy is the local spin density (LSD) approximation [1], which is valid for densities that vary slowly over space:

$$E_{XC}^{LSD}[\,\rho_\uparrow, \rho_\downarrow\,] = \int d^3r\, \rho(\mathbf{r})\varepsilon_{XC}\big(\,\rho_\uparrow(\mathbf{r}), \rho_\downarrow(\mathbf{r})\big),$$

where ε_{XC} is the exchange–correlation energy per particle of an electron gas with homogeneous spin densities $\rho_\uparrow$ and $\rho_\downarrow$, and $\rho = \rho_\uparrow + \rho_\downarrow$. Although the densities of real systems vary rapidly on the scale of the local Fermi wavelength [$2\pi/k_F$, where $k_F = (3\pi^2\rho)^{1/3}$] and Thomas–Fermi screening length, LSD is still moderately accurate due to its satisfaction of important constraints [2] on the exact exchange–correlation hole. Typically, LSD makes useful predictions for the geometry and elastic properties of molecules and solids, but overestimates atomization energies.

The Perdew–Wang 1991 (PW91) [3–5] generalized gradient approximation (GGA) incorporates additional information from the electron gas of slowly varying but nonconstant density, while enforcing the same exact hole constraints as LSD; other GGAs are also available and are used in the literature [6–8]. They may all be cast in the useful form [9]

$$E_{XC}^{GGA}[\,\rho_\uparrow, \rho_\downarrow\,] = \int d^3r\, \rho(\mathbf{r})\varepsilon_{XC}(r_s(\mathbf{r}), \zeta(\mathbf{r}), s(\mathbf{r})), \quad (1)$$

where $r_s(\mathbf{r}) = [3/4\pi\rho(\mathbf{r})]^{1/3}$ and $\zeta(\mathbf{r}) = [\,\rho_\uparrow(\mathbf{r}) - \rho_\downarrow(\mathbf{r})]/\rho(\mathbf{r})$.[†] The important new ingredient beyond LSD is the reduced or dimensionless density gradient

$$s = \frac{|\nabla\rho|}{2k_F\rho}.$$

[†]We ignore the small $\nabla\zeta$ terms that arise from exact spin-scaling of E_X [10] and that are negligible for the systems discussed here.

In fact, for a GGA which recovers the uniform-gas limit, such as PW91, LSD is just Eq. (1) with $\varepsilon_{XC}(r_s, \zeta, s)$ replaced by $\varepsilon_{XC}(r_s, \zeta, 0)$. GGA seem most reliable for $s \leq 1$ and least so for $s > 3$.

The PW91 GGA is the ''most local'' of the GGAs [9] and the only one constructed entirely from first principles[‡] [5]. It yields significant improvements over LSD in atomization energies and reaction barriers for almost all systems [11] and in the geometries, elastic properties, and magnetic properties of many metals [12]. For bulk semiconductors, where LSD gives unusually accurate elastic constants and bulk moduli, GGA leads to some worsening [13–15] and some improvement [16] relative to LSD. Thus, a better understanding is needed of the systems and properties for which LSD and GGA are the most or least suitable. Such an understanding could guide future applications and perhaps lead to further improvements in density functionals. In this work, we present an analysis of the exchange–correlation functionals by decomposing them into contributions from their ingredients r_s, ζ, and s as a possible step in this direction. We also show results of this analysis applied to atoms and ions. In future work [17], we will present results for molecules and solids.

This article is divided into three parts: In the first section, we explain the partitioning scheme for the electron density. In the second, we set forth the computational aspects of this work. In the last section, we present the results and discussion. We use atomic units throughout ($e^2 = \hbar = m = 1$).

Density Functions

For an analysis of any electron density, we define the density function

$$g(r_s, \zeta, s) = \frac{3}{4\pi r_s^3}\int d^3r\, \delta(r_s - r_s(\mathbf{r}))\,\delta(\zeta - \zeta(\mathbf{r}))\,\delta(s - s(\mathbf{r})), \quad (2)$$

where $r_s(\mathbf{r})$, $\zeta(\mathbf{r})$, and $s(\mathbf{r})$ denote the Seitz radius, relative spin polarization, and reduced density gradient at point $\mathbf{r}$, respectively.

The function $g(r_s, \zeta, s)$ of three variables contains sufficient information to evaluate any GGA

[‡]In [3, 5], a numerically defined GGA is defined via real-space cutoff of the spurious long-range part of the gradient expansion for the exchange–correlation hole, with no empirical bias. The *analytic fit* to the exchange component of this functional contains a slight empirical bias.

for the energy as

$$E_{XC}^{GGA} = \int d^3r\, \rho(\mathbf{r})\, \varepsilon_{XC}^{GGA}(r_s(\mathbf{r}), \zeta(\mathbf{r}), s(\mathbf{r})) = \int_0^\infty dr_s \int_{-1}^{1} d\zeta \int_0^\infty ds\, g(r_s, \zeta, s) \times \varepsilon_{XC}^{GGA}(r_s, \zeta, s).$$

Note that our normalization is chosen so that

$$\int_0^\infty dr_s \int_{-1}^{1} d\zeta \int_0^\infty ds\, g(r_s, \zeta, s) = \int d^3r\, \rho(\mathbf{r}) = N \quad (3)$$

and that $g(r_s, \zeta, s)\, dr_s\, d\zeta\, ds$ is the average number of electrons in regions of space, where $r_s(\mathbf{r})$ is between r_s and $r_s + dr_s$, $\zeta(\mathbf{r})$ between ζ and $\zeta + d\zeta$, and $s(\mathbf{r})$ between s and $s + ds$. N is the number of electrons in the system.

Since it is difficult to visualize and understand a function of three variables, we define three auxiliary functions of one variable, where two of the variables are analytically integrated out:

$$g_1(r_s) = \int_{-1}^{1} d\zeta \int_0^\infty ds\, g(r_s, \zeta, s), \quad (4a)$$

$$g_2(\zeta) = \int_0^\infty dr_s \int_0^\infty ds\, g(r_s, \zeta, s), \quad (4b)$$

$$g_3(s) = \int_0^\infty dr_s \int_{-1}^{1} d\zeta\, g(r_s, \zeta, s), \quad (4c)$$

so that

$$\int_0^\infty dr_s\, g_1(r_s) = \int_{-1}^{1} d\zeta\, g_2(\zeta) = \int_0^\infty ds\, g_3(s) = N.$$

Note that knowledge of g_1, g_2, and g_3 alone is insufficient to reconstruct the full $g(r_s, \zeta, s)$ and, thus, the GGA energy.

For a specific GGA energy functional, we can also define the energy-weighted density function

$$f_{XC}^{GGA}(r_s, \zeta, s) = \varepsilon_{XC}^{GGA}(r_s, \zeta, s)\, g(r_s, \zeta, s), \quad (5)$$

so that

$$\int_0^\infty dr_s \int_{-1}^{1} d\zeta \int_0^\infty ds\, f_{XC}^{GGA}(r_s, \zeta, s) = E_{XC}^{GGA}.$$

Equivalently, as for the electron density analysis in Eqs. (4), we define auxiliary functions for the energy-weighted density function of Eq. (5):

$$f_1(r_s) = \int_{-1}^{1} d\zeta \int_0^\infty ds\, f_{XC}^{GGA}(r_s, \zeta, s), \quad (6a)$$

$$f_2(\zeta) = \int_0^\infty dr_s \int_0^\infty ds\, f_{XC}^{GGA}(r_s, \zeta, s), \quad (6b)$$

$$f_3(s) = \int_0^\infty dr_s \int_{-1}^{1} d\zeta\, f_{XC}^{GGA}(r_s, \zeta, s), \quad (6c)$$

so that

$$\int_0^\infty dr_s\, f_1(r_s) = \int_{-1}^{1} d\zeta\, f_2(\zeta) = \int_0^\infty ds\, f_3(s) = E_{XC}^{GGA}.$$

All these decompositions of E_{XC}, performed for different systems and different functionals, should yield useful physical insight into the structure of the electron density. In fact, independently of this work, Moll et al. [16] already used the r_s-analysis to explain their LSD and GGA results for the pressure at which Si transforms from the diamond structure. Furthermore, Philipsen and Baerends [18] used the s-analysis to investigate the importance of the small-s regime ($s \ll 1$) for GGA energies of solids.

Computational Method

To obtain a computationally tractable formula for the g and f functions [Eqs. (4) and (6)], one inserts the definition of the density function $g(r_s, \zeta, s)$ of Eq. (2) into either of Eqs. (4) or (6) and changes the order of the integration. For example, in the case of the reduced-gradient analysis, we find that

$$g_3(s) = \int d^3r\, \rho(\mathbf{r})\, \delta(s - s(\mathbf{r})), \quad (7)$$

with analogous results for either the r_s-analysis or the ζ-analysis. A direct numerical integration over the complete three-dimensional space of the Dirac delta function in Eq. (7) is impossible due to the limited accuracy of the integration grid.

However, one define a function

$$N(s) = \int d^3r\, \rho(\mathbf{r})\, \theta(s - s(\mathbf{r})), \quad (8)$$

where $\theta(s)$ is the Heaviside step function. The physical interpretation of (8) is straightforward: $N(s)$ is the number of electrons that have a reduced gradient between 0 and s, and $dN(s)/ds = g_3(s)$.

We may avoid the numerical noise in integration (8) due to the discontinuity of the θ function at $s = s(\mathbf{r})$. We replace the θ function by a function with smooth edges. The Fermi–Dirac distribution function at finite temperature has the desired properties:

$$\theta(s - s(\mathbf{r})) \to \frac{1}{\exp(-(s - s(\mathbf{r}))/T) + 1}.$$

The ''temperature'' T is chosen as small as possible, while avoiding visible noise in our figures due to the integration grid, with a value usually between 0.005 and 0.03.[§]

For spherically symmetric systems, we can also easily calculate the exact (or zero-temperature) functions. In such a case, the integral in Eq. (7) runs over a single variable, $r = |\mathbf{r}|$, becoming

$$g_3(s) = 4\pi \int_0^\infty dr\, r^2\, \rho(r)\, \delta(s - s(r)). \qquad (9)$$

Now, a change of variables in the δ-function from s to r yields

$$g_3(s) = 4\pi \sum_i \frac{r_i^2 \rho(r_i)}{|s'(r_i)|}, \qquad (10)$$

where $s'(r) = ds/dr$ and the sum runs over all solutions of the equation $s(r_i) = s$.

In Figure 1 we study the effect of the broadening due to finite temperature, by plotting both the zero-temperature and finite-temperature $g_3(s)$ curves for a Li atom. The dashed curve on this plot is calculated with $T = 0.03$, and the solid line is a zero-temperature function. (The finite-temperature curve reappears sideways as the solid line in the bottom-right panel of Fig. 3, and a detailed discussion of its shape is reserved for the fourth section.) Notice that only near the peaks do the two curves differ and then only slightly. Furthermore, the area under the sharp peaks is small, an observation most easily made from the temperature-broadened curve.

With this approximation, we can calculate g and f functions for different systems. In the present work, we treat only spherically symmetric atoms, which leads to the further simplification of Eq. (9). In view of the later extension of our work to more complicated systems (molecules, solids), we chose instead to keep our method as general as possible, so we used a full three-dimensional multicenter integration method with Becke's weights [19], including Lebedev angular [20, 21] and Gauss–Legendre radial integration. For the results of this article, we used 1600 points per atom in the radial direction and, according to the symmetry, the lowest accuracy of the Lebedev scheme in the angular integration.

We employed a computational package to perform the integrals here, anticipating the extension of this work to other systems. We used the CRYSTAL program [22, 23] with the DFT extension [24], which can treat both finite systems and systems which are infinite in one, two, and three dimensions. As the input densities, we used Hartree–Fock electronic densities for atoms expanded in Slater-type-orbitals, as calculated by Clementi and Roetti [25].

Results and Discussion

We performed our density-gradient analysis for a number of atoms and ions. In this work, we present typical examples. As an example of a closed-shell system, we chose an Ar atom. For the study of ionization, we chose the Li atom and the Li^+ ion.

We center the atom at $r = 0$. Where the density decays exponentially (approximately true within a shell), $r_s(r)$ and $s(r)$ grow exponentially. To make the interpretation of the density functions easier, we separate the density functions into contributions from different regions of space. The key plot is $s(r)$ (see Figs. 2 and 3 for the Ar and Li atoms, respectively), which splits the r-space into four domains:

- **Pure core region:** From $r = 0$ to the r for the outermost maximum of $s(r)$ (left black dot). This region contains all core electrons not in the core–valence transition region. It includes the space close to the nucleus where $\rho(\mathbf{r}) \approx (2Z^3/\pi)\exp(-2Zr)$, making $s(0) \approx 0.38$ and $r_s(0) \approx 0.72/Z$, where Z is the nuclear charge.
- **Core–valence (CV) transition region:** From the r for the outermost maximum of $s(r)$ to the r for the outermost minimum of $s(r)$ (right black dot). This region is a thin shell in real space between the pure core and pure valence regions. In this region, the core– and

[§]We use a value of 0.01 for Ar and 0.03 for Li and Li^+.

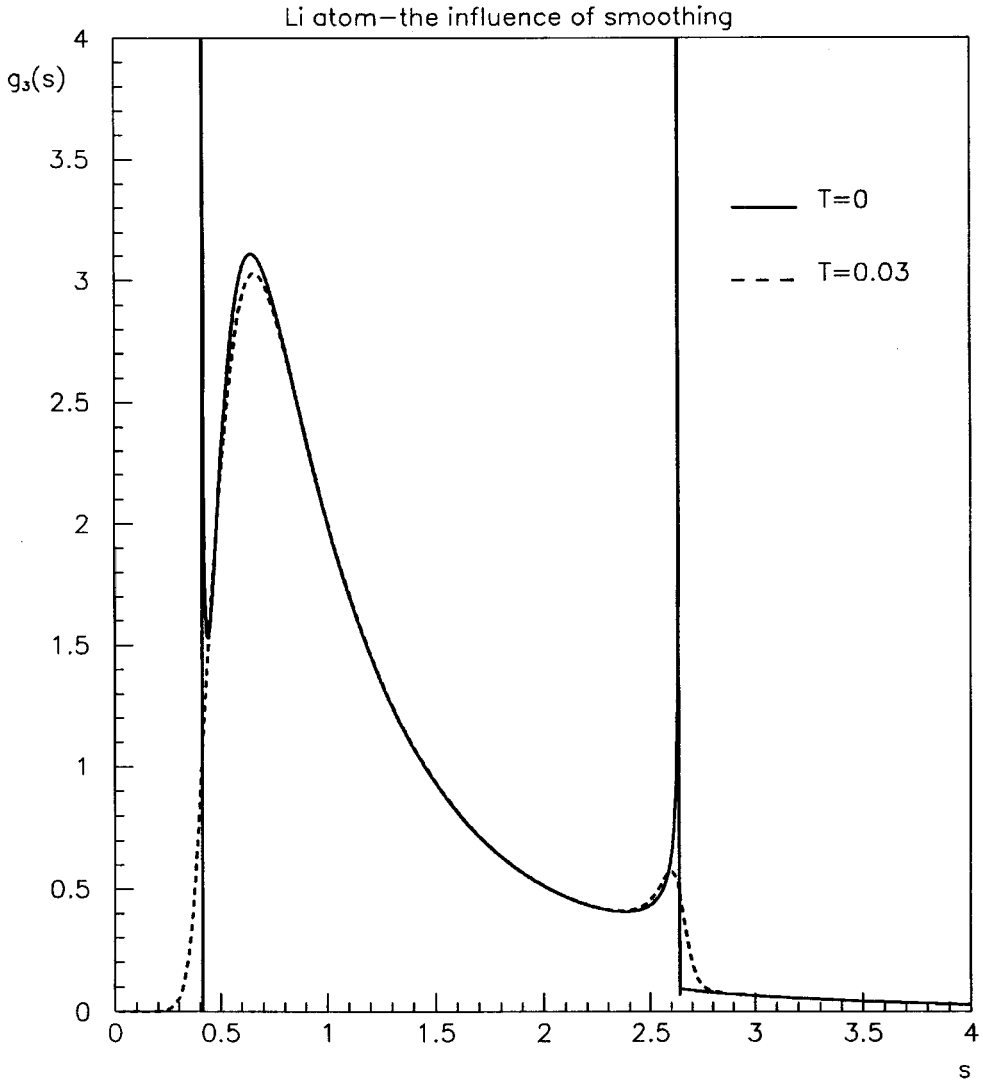

FIGURE 1. The influence of the Fermi–Dirac smoothing function on the integration for the Li atom. The solid line represents the zero-temperature result and the dashed line represents the result for $T = 0.03$. The difference can be seen only in the sharp peaks; the smooth part of $g_3(s)$ remains unaffected. The area under $g_3(s)$ is three electrons.

valence–electron densities are of comparable size.

- **Pure valence region:** From the r for the outermost minimum of $s(r)$ to the r where $s(r)$ passes through the value it takes at its greatest maximum. We call this the pure valence region, because it includes those contributions from the outermost shell whose reduced density gradients are comparable to those in the core.
- **Tail region:** The rest of space, in which s increases monotonically up to ∞ as $r \to \infty$. Only for the sake of the $g_3(s)$ analysis do we need to distinguish the tail from the valence region.

On the density-gradient analysis plots (Figs. 2 and 3), vertical dashed lines define the regions of space discussed above. Horizontal dashed lines indicate which parts of the g density functions belong to which spatial region (Figs. 2 and 3). In

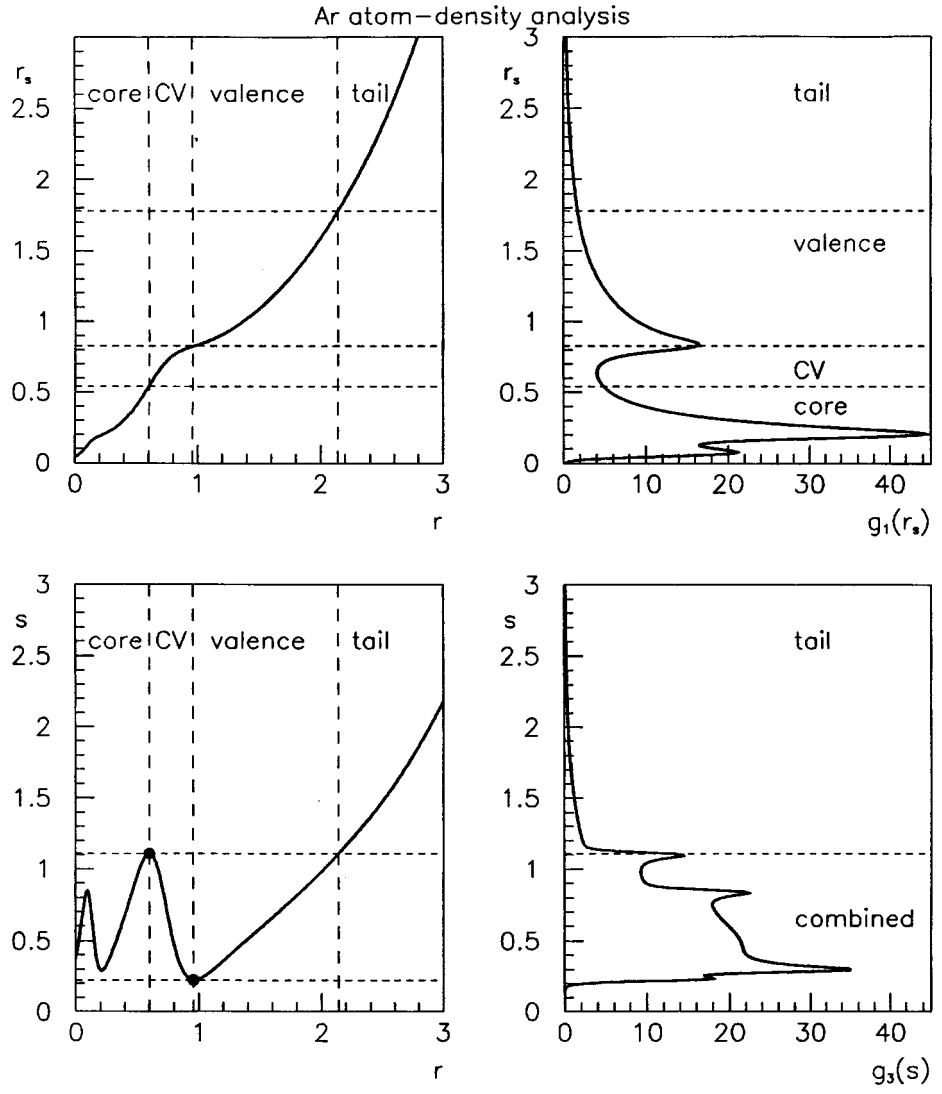

FIGURE 2. Density-gradient analysis for the Ar atom. The bottom-left plot of $s(r)$ determines the partitioning of r-space into regions as discussed in the text. The top-left plot shows $r_s(r)$, while the plots on the right represent $g_1(r_s)$ and $g_3(s)$. The atom is centered at $r = 0$. The areas under $g_1(r_s)$ and $g_3(s)$ are both 18 electrons. The pure core, core−valence, pure valence, and tail regions contain 9.34, 1.75, 5.37, and 1.54 electrons, respectively.

Figure 3, the results for the Li^+ ion are also depicted, using a dot−dashed line.

Since r_s is a monotonic function of r, these regions in r-space have a one-to-one correspondence with intervals in r_s-space. Because $s(r)$ is not monotonic, there is typically a "combined" region in the s-analysis, in which contributions from core and valence electrons are superposed. This region ends abruptly as the s of the greatest maximum, so there is a sharp step in $g_3(s)$ that separates the contribution from the core−valence region (where s typically achieves its greatest maximum) from that of the tail.

Plots of the reduced-density gradient $s(r)$ vs. r (Figs. 2 and 3) clearly distinguish each pure atomic shell [a region in which $s(r)$ is an increasing function of r] and each transition region between shells [in which $s(r)$ is a decreasing function of r]. The

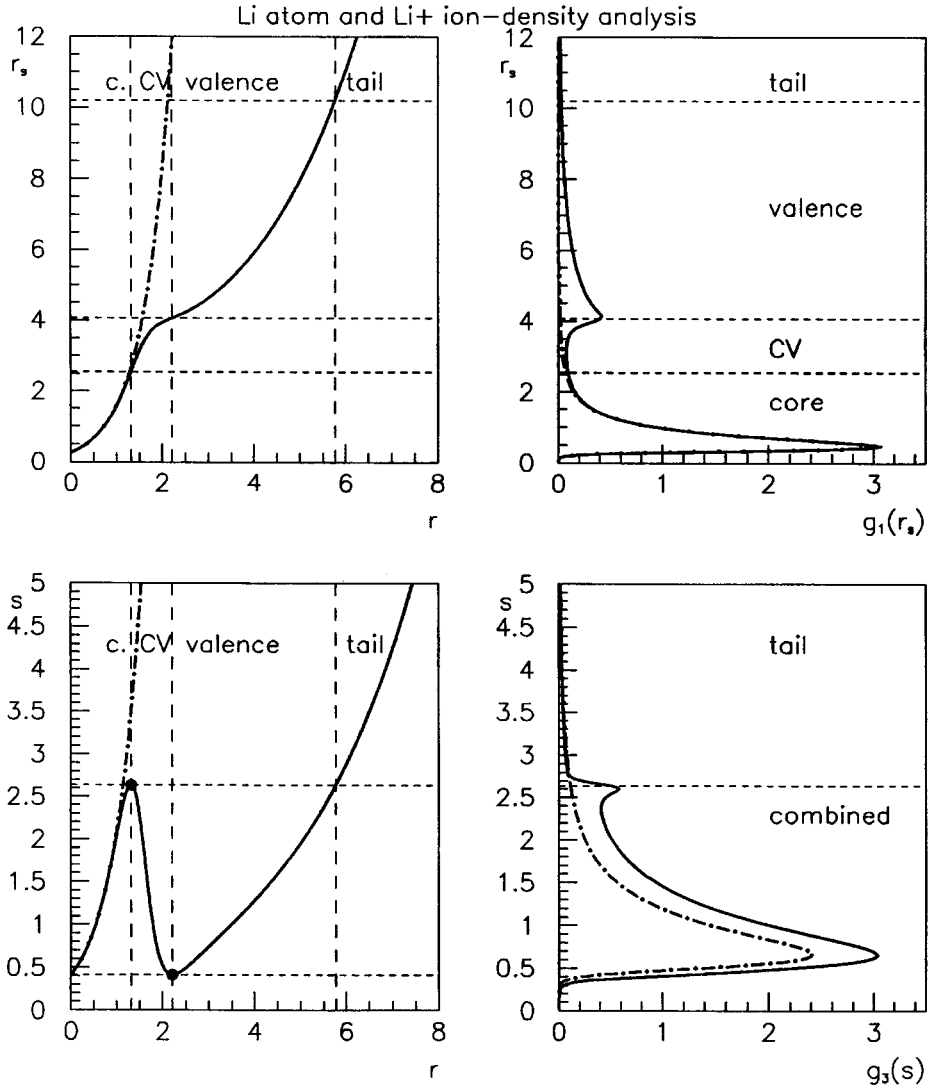

FIGURE 3. Density-gradient analysis for (solid line) the Li atom and (dash−dot line) the Li^+ ion. The difference between atom and ion in the r_s-analysis can be seen only on the core−valence, pure valence, and tail regions. The pure core, core−valence, pure valence, and tail regions contain 1.94, 0.19, 0.75, and 0.12 electrons for the Li atom, and 1.925, 0.073, 0.002, and 0.00 electrons for the Li^+ ion, respectively.

number of electrons in the pure core, core−valence, pure valence, and tail regions are reported in the figure captions. If we attribute half the electrons in the core−valence transition region to the core and the other half to the valence, then we obtain almost the conventional number of electrons in the core (10.22 for Ar, 2.04 for Li, and 1.96 for Li^+, using the same boundaries for Li^+ as for Li). The radii of the spheres containing the number of core electrons states above are 0.78 and 1.76 bohrs for Ar and Li, respectively, which is consistent with the numbers of Schmider et al. [26], who have calculated ''ideal shell radii'' which encompass the conventional number of electrons in each shell (0.72 and 1.53 bohrs for Ar and Li core radii, respectively). Note that Kohout et al. [27] used the nonreduced density gradient $|\nabla\rho|/\rho$ to distinguish the atomic shells.

In Figures 4 and 5, we plot the density of the exchange–correlation energy f. The solid line denotes the f function with LSD exchange–correlation energy ε_{XC} (Dirac's exchange energy [28] and a parametrization of the LSD correlation energy [29]), and the dashed line denotes the GGA exchange–correlation energy of Perdew–Wang 1991 [3–5]. For the Li^+ ion, we plot in Figure 6 the difference between f functions for the Li atom and the Li^+ atom.

From these figures, some common features of the density functions can be obtained: We see that the r_s dependence of the g and f curves starts at r_s^{min}, which corresponds to the maximum electronic density at the atomic center. The $g_1(r_s)$ function also clearly shows the shell structure of the atom, the number of peaks corresponding to the number of fully or partially occupied shells in the atom. In the tail region, the g and f curves fall rapidly to zero. The r_s curves for the atom and ion

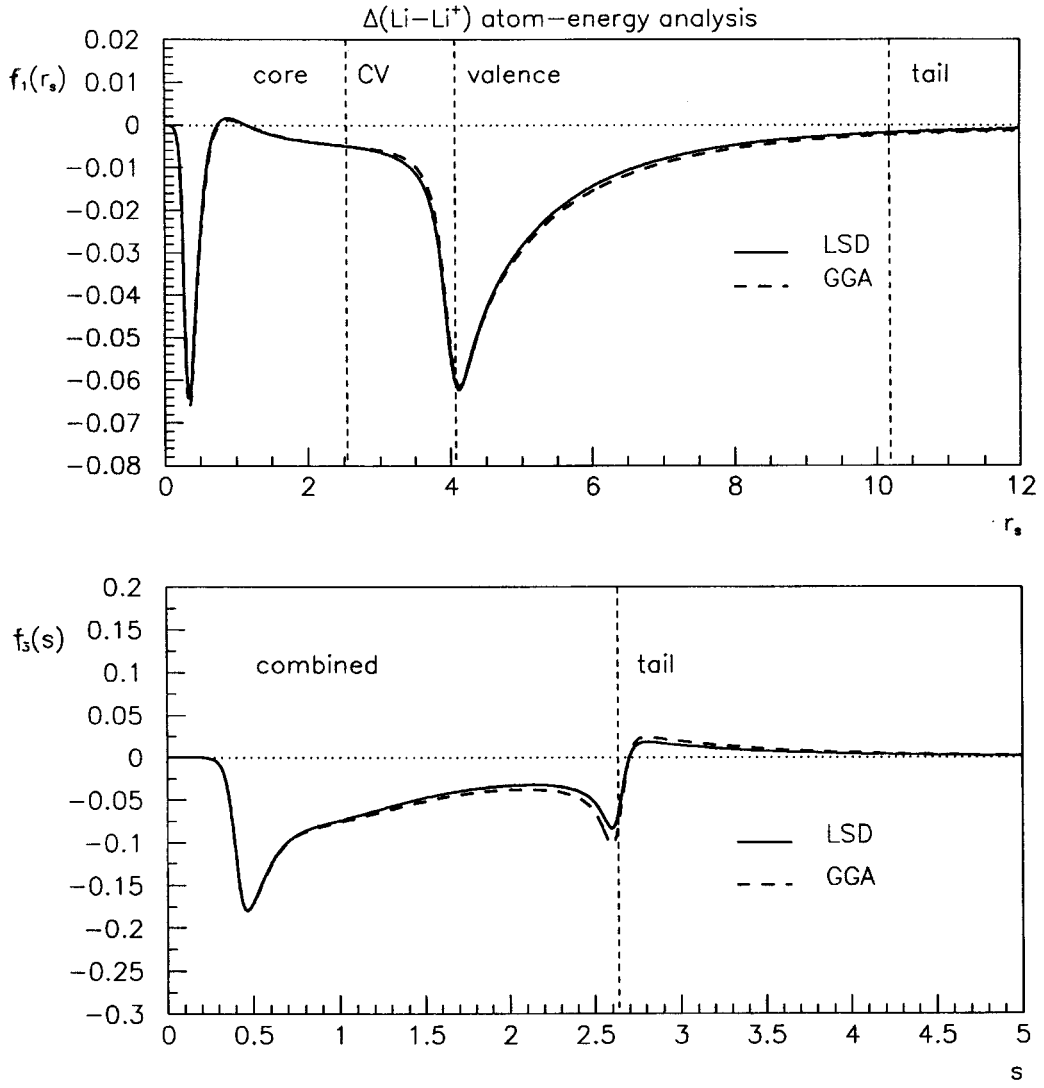

FIGURE 6. Energy-weighted density-gradient analysis for the Li^+ ion. The difference Δf between the Li atom and Li^+ ion is plotted. The top plot shows the r_s-analysis of the exchange–correlation energy, and the bottom, the s-analysis. The solid line was obtained with the LSD approximation for the exchange–correlation energy, and the dashed line, with the GGA approximation. The area under $\Delta f_1(r_s)$ [or $\Delta f_3(s)$] is -0.134 Hartree (LSD) or -0.139 Hartree (GGA).

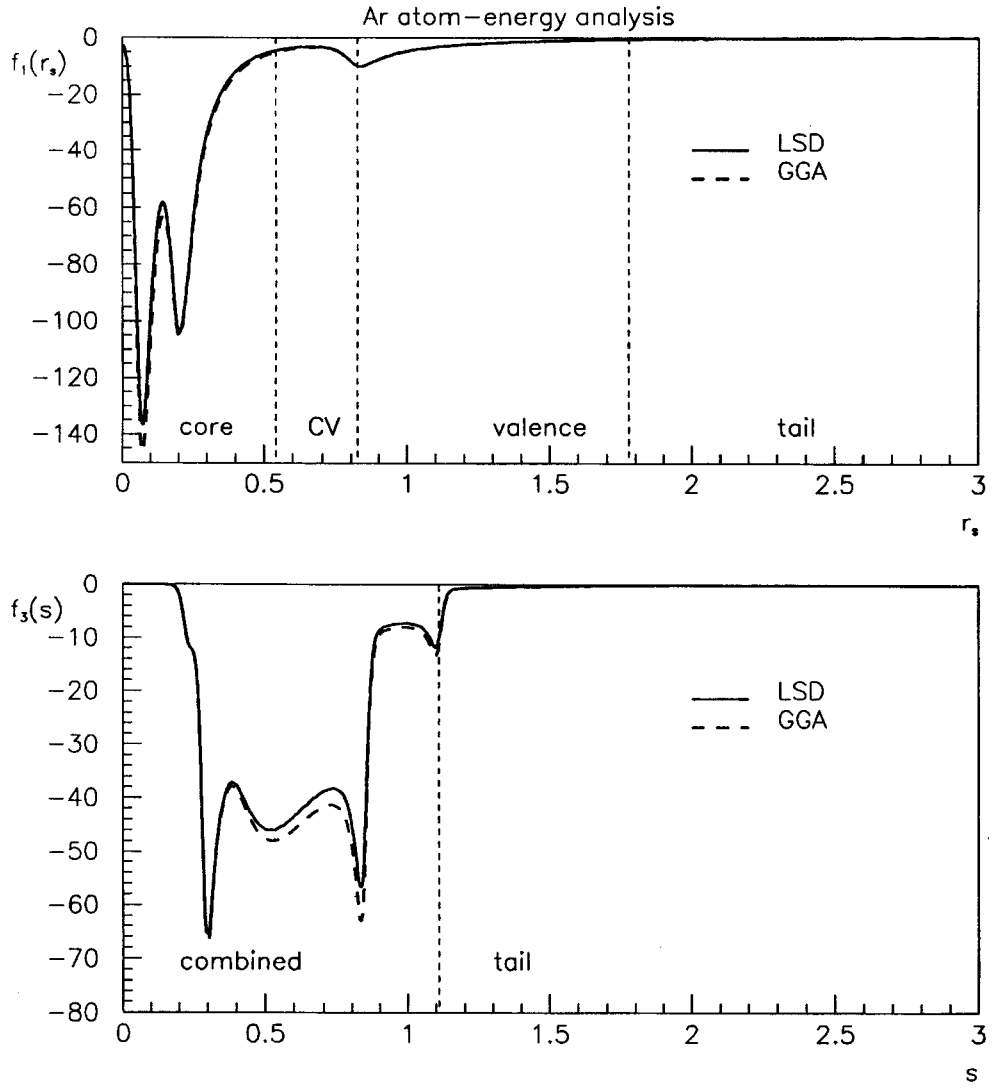

FIGURE 4. Energy-weighted density-gradient analysis for the Ar atom. The top plot shows the r_s-analysis of the exchange–correlation energy, and the bottom, the s-analysis. The solid line was obtained with the LSD approximation for the exchange–correlation energy, and the dashed line, with the GGA approximation. The area under $f_1(r_2)$ [or $f_3(s)$] is −29.29 Hartrees (LSD) or −30.89 Hartrees (GGA).

are very similar in the pure core region, whereas they differ significantly in the core–valence, pure valence, and tail regions; the same similarity between the atom and ion holds for the pure core region of the $g_1(r_s)$ curve.

In the $s(r)$ plots, we observe that each shell has its minimum (s^{min}) and maximum (s^{max}) values. For each s^{min} and s^{max}, we obtain a peak in the curves of g and f vs. s. The g and f curves fall rapidly to zero beyond the largest s^{max} of all the shells. The separation of space into different regions is not so clear in the s- as in the r_s-analysis.

We may conclude from this analysis that only the ranges $0 < r_s < 10$ and $0 < s < 3$ are important for the energy E_{XC} in atoms. Thus, the low-density ($r_s > 10$) and large-gradient ($s > 3$) domains, where GGAs are least trustworthy, are not tested in atoms. In closed-shells like noble gases, only the range $s < 1.5$ is important. Large-s contributions include a substantial contribution from the

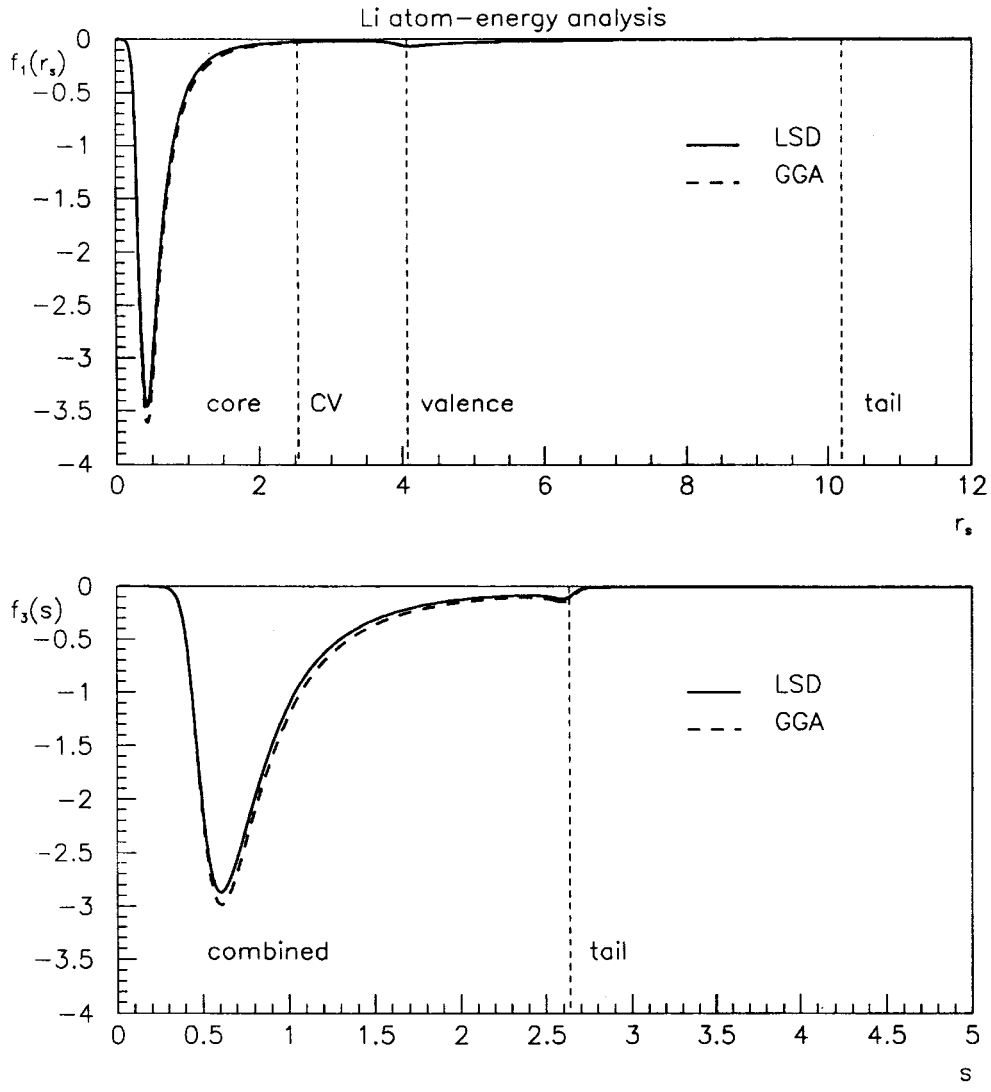

FIGURE 5. Energy-weighted density-gradient analysis for the Li atom. The top plot shows the r_s-analysis of the exchange−correlation energy, and the bottom, the s-analysis. The solid line was obtained with the LSD approximation for the exchange−correlation energy, and the dashed line, with the GGA approximation. The area under $f_1(r_s)$ [or $f_3(s)$] is −1.69 Hartrees (LSD) or −1.82 Hartrees (GGA).

inner boundary of the core−valence region. This region is present not only in atoms but also in molecules and solids and may be responsible for some of the LSD or GGA errors in those systems.

Figure 6 suggests that a significant fraction of the change in E_{XC} under ionization arises in the core. However, in a self-consistent calculation, this contribution should be canceled [30] by the changes in other energy components within the core.

ACKNOWLEDGMENTS

A.Z. wishes to thank the Slovenian Ministry of Science and Technology for financial support of his Ph.D. studies and the Tulane Physics Department where part of this work was performed. This work was supported by National Science Foundation Grant DMR95-21353 at Tulane.

References

1. W. Kohn and L. J. Sham, Phys. Rev. A **140**, 1133 (1965).
2. R. M. Dreizler and E. K. U. Gross, *Density Functional Theory: An Approach to the Quantum Many Body Problem* (Springer-Verlag, Berlin, 1990); R. G. Parr and W. Yang, *Density-Functional Theory of Atoms and Molecules* (Oxford University Press, Oxford, 1989).

3. J. P. Perdew, in *Electronic Structure of Solids '91*, P. Ziesche and H. Eschrig, Eds. (Akademie Verlag, Berlin, 1991), pp. 11−20.
4. J. P. Perdew, J. A. Chevary, S. H. Vosko, K. A. Jackson, M. R. Pederson, D. J. Singh, and C. Fiolhais, Phys. Rev. B **46**, 6671 (1992); *Ibid*. **48**, 4978 (1993).
5. J. P. Perdew, K. Burke, and Y. Wang, submitted.
6. J. P. Perdew, Phys. Rev. B **33**, 8822 (1986); *Ibid*. **34**, 7406 (1986).
7. A. D. Becke, Phys. Rev. A **38**, 3098 (1988).
8. C. Lee, W. Yang, and R. G. Parr, Phys. Rev. B **37**, 785 (1988).
9. J. P. Perdew and K. Burke, Int. J. Quantum Chem. **57**, 309 (1996).
10. G. O. Oliver and J. P. Perdew, Phys. Rev. A **20**, 397 (1979).
11. K. Burke, J. P. Perdew, and M. Levy, in *Modern Density Functional Theory: A Tool for Chemistry*, J. M. Seminario and P. Politzer, Eds. (Elsevier, Amsterdam, 1995).
12. V. Ozoliņš and M. Körling, Phys. Rev. B **48**, 18304 (1993).
13. C. Filippi, D. J. Singh, and C. Umrigar, Phys. Rev. B **50**, 14947 (1994).
14. M. Causà and Z. Zupan, Int. J. Quantum Chem. **S28**, 633 (1994).
15. A. Zupan and M. Causà, Int. J. Quantum Chem. **56**, 337 (1995).
16. N. Moll, M. Bockstedte, M. Fuchs, E. Pehlke, and M. Scheffler, Phys. Rev. B **52**, 2550 (1995).
17. A. Zupan, J. P. Perdew, K. Burke, and M. Causá, unpublished.
18. P. H. T. Philipsen and E. J. Baerends, private communication.
19. A. D. Becke, J. Chem. Phys. **88**, 2547 (1988).
20. V. I. Lebedev, Zh. Vychisl. Mat. Mat. Fiz. **16**, 293 (1976).
21. V. I. Lebedev, Sibirsk. Mat. Zh. **18**, 132 (1977).
22. R. Dovesi et al., CRYSTAL 88, QCPE Program No. 577 (Bloomington, IN, 1989).
23. R. Dovesi, V. R. Saunders, and C. Roetti, Technical Report (University of Torino, 1992).
24. M. Towel, M. Causà, and A. Zupan, submitted.
25. E. Clementi and C. Roetti, At. Data Nucl. Data Tab. **14**, 177 (1974).
26. H. Schmider, R. P. Sagar, and V. H. Smith, Jr., J. Chem. Phys. **94**, 8627 (1991); *Ibid*., Can. J. Chem. **70**, 506 (1992).
27. M. Kohout, A. Savin, and H. Preuss, J. Chem. Phys. **95**, 1928 (1991).
28. P. A. M. Dirac, Proc. Camb. Philos. Soc. **26**, 376 (1930).
29. J. P. Perdew and Y. Wang, Phys. Rev. B **45**, 13244 (1992).
30. U. von Barth and C. D. Gelatt, Phys. Rev. B **21**, 2222 (1980).